Nuclear Instruments and Methods in Physics Research B 566 (2025) 165773

Contents lists available at ScienceDirect

Nuclear Inst. and Methods in Physics Research, B

journal homepage: www.elsevier.com/locate/nimb

Full length article

Assessing the near-surface diffusion of Xe and Kr in Zirconia by time-of-flight elastic recoil detection analysis

N. Wikström [a,b], M. Giamouridou [b], E. Charatsidou [b], P. Olsson [b], J. Oscarsson [c], D. Primetzhofer [a,c], R.J.W. Frost [a,*]

[a] Department of Physics and Astronomy, Uppsala University, Uppsala, Sweden
[b] Department of Physics, KTH Royal Institute of Technology, Stockholm, Sweden
[c] The Tandem Laboratory, Uppsala University, Uppsala, Sweden

ARTICLE INFO

Keywords:
ToF-ERDA
Fission product
Nuclear fuel
Fick's law
Radiation Damage

ABSTRACT

The diffusion of two volatile fission products, xenon (Xe) and krypton (Kr), in zirconia (ZrO_2) is investigated. Samples of Yttria (Y_2O_3)-stabilised tetragonal ZrO_2 were implanted with either Xe or Kr, at 300 keV, with a fluence of 10^{17} at./cm^2, and subsequently analysed with time-of-flight elastic recoil detection analysis (ToF-ERDA) to obtain elemental composition depth profiles. Samples were then annealed at 1200 °C for 9 h, and the effect of the annealing was assessed by ToF-ERDA measurements. From these measurements, first-order approximations of diffusion coefficients for Xe and Kr in ZrO_2 were derived, using a model based on Fick's second law, these being $(1.36 \pm 0.87) \times 10^{-19}$ m^2/s and $(2.94 \pm 1.96) \times 10^{-19}$ m^2/s at 1200 °C for Kr and Xe respectively. It was shown that ToF-ERDA can provide data to analyse the diffusion of elements in solid sample matrices and that a model based on Fick's Law can predict the diffusion of the implanted ions.

1. Introduction

The diffusion of gaseous fission products such as Xe and Kr, in nuclear fuel, has significant impact on reactor performance and safety parameters, due to high fission-yields, high neutron absorption cross-sections [1] and the potential to create pressure build-up within the fuel cladding [2,3]. The study of the diffusion behaviour of noble gaseous species is, however, an experimental challenge, due to difficulties in incorporating gaseous species in the fuel matrix as well as in accessing techniques which can monitor gas concentrations and diffusion on ultrashort-length scales [4,5]. In the majority of cases, diffusion parameters are derived from irradiated materials [6], either through measurements in the plenum, or by exposure in materials test reactors and post-irradiation examination facilities. Traditional measurement methods include: Thermal-Desorption Spectrometry (TDS) [7], although this may only measure induced gas release during annealing; and Secondary Ion Mass Spectrometry (SIMS) [8] which, despite providing elemental depth profiles, is a destructive technique and limited largely to qualitative analysis. Although effective, the use of irradiated materials requires significant infrastructure and resources to operate, and thus limits sample throughput.

The behaviour and diffusion of gaseous fission products are complex, and studies are numerous [7,9–12]. Due to the existence of mechanisms such as burst release [12] and gas-atom trapping along the diffusion path [7], parameters such as radiation damage, gas atom drift [11] and lattice structure must be considered, alongside thermal diffusion. It has been suggested that gas-atoms drift along dislocations in fuel, causing an increase in the diffusion of gaseous fission products towards the surface [11]. Furthermore, radiation damage can increase the trapping of gas atoms in fuel matrix defects, and cause further reduction of concentration when the trapped atoms are released [7]. Finally, heat treatment of fuel with implanted atoms can cause burst-release [7], in which a fraction of the implanted element rapidly diffuses to the surface as annealing is started, and is released from the fuel matrix [12]. As gaseous fission products usually have low solubility in nuclear fuel, they also have the tendency to form gas bubbles, which diffuse differently compared to individual gas atoms [9,10]. This multitude of possible mechanisms, both thermal and athermal, makes modelling the diffusion of volatile fission products extremely challenging [13]. Some studies have evaluated the modelling of fission product diffusion using Fick's law [7,11], proposing to modify Fick's second law to account for radiation damage, gas release and lattice structure. In the present work, a similar but somewhat simpler model was employed, although unlike previous studies was based on measurements of elemental depth-profiles, rather than simulated data.

* Corresponding author.
E-mail address: rob.frost@physics.uu.se (R.J.W. Frost).

https://doi.org/10.1016/j.nimb.2025.165773
Received 2 October 2024; Received in revised form 29 May 2025; Accepted 6 June 2025
Available online 25 June 2025

Generation-IV nuclear reactors may use fuels other than uranium dioxide (UO_2) [14,15], with one possible alternative being thorium dicarbide (ThC_2) [16]. ThC_2 is most stable in a monoclinic or tetragonal structure [17], but will exist in a purely tetragonal state at reactor operating temperatures between 1430 °C–1480 °C [18], with a calculated thermal conductivity of 5 W/mK at room temperature [19–22]. Yttria (Y_2O_3)-stabilised tetragonal zirconia (ZrO_2) represents a surrogate material for ThC_2, as both show similar crystal structures and thermal conductivities. Tetragonal zirconia thus makes a good candidate for studying the diffusion of volatile fission products, such and Xe and Kr, in this advanced reactor fuel type. Additionally, the diffusion of volatile elements in ZrO_2 is of interest, in the more general context of reactor operation, as many nuclear reactors utilise Zr in the cladding tubes which oxidise during operation [23]. ZrO_2 has also been utilised in a composite with UO_2 as seed fuel in the second core of the Shippingport Reactor [24].

Presented here is an extension of previous work [25], combining medium-energy ion implantation with time-of-flight elastic recoil detection analysis (ToF-ERDA), to investigate the diffusion of volatile elements in high-density sample matrices. ZrO_2 samples were implanted with Kr and Xe, and the depth-dependent concentrations of these elements measured before the samples were annealed and the depth-dependent concentrations were measured again. A model employing Fick's second law and a sink term, was then fitted to the experimentally measured Xe and Kr depth profiles, to obtain values for the diffusion coefficients at the annealing temperature. This work contributes towards providing benchmarking data for the validation of short-length scale atomistic models, such as those built upon the use of density functional theory [26,27] and semi-empirical potential driven molecular dynamics, which in turn contribute significantly to the Accelerated Fuel Qualification initiative [28]. The technique described here has the potential to significantly reduce the cost and timescale of new fuel qualification when compared to traditional methods.

2. Method

2.1. Overview

The experimental methodology used in the present study, a schematic illustration of which is presented in Fig. 1, follows that previously applied to the study of Kr diffusion in UO_2 and ADOPT® [25]. Elements of interest are introduced into the near surface of samples through ion implantation, with energies typically in the range of several keV/amu. ToF-ERDA is then used to assess the depth-dependent concentration profiles of the implanted elements. By annealing the samples for a suitable duration, at a suitable temperature, and then re-measuring concentration depth profiles for the elements of interest, information on the diffusion of these elements can be obtained.

2.2. Samples

Samples used in the present study were formed from DeCore®Solid A1 ZrO_2, stabilised in the tetragonal phase with 3 mol% Y_2O_3. Samples were cuboid in shape, with approximate dimensions of 5 mm by 5 mm by 20 mm. The two smaller faces of each sample were roughly cut, with the remaining four faces of each were ground and polished prior to delivery by the manufacturer. An image of one of the samples, after being subject to the process described in Section 2.1, is presented in Fig. 2.

Each sample was weighed in both air and chloroform and Archimedes' principle was applied, yielding a density of 6.005 g/cm^3 for the material, which corresponds to 99% theoretical density [29]. The lattice parameters were measured using X-ray diffraction and showed a tetragonal structure with a = b = 3.6014 ± 0.0003 Å and c = 5.1717 ± 0.0005 Å.

2.3. Ion implantation

Ion implantations were performed using the 350 kV high-current Danfysik 1090 accelerator platform at the Tandem Laboratory, Uppsala University [30]. One sample was implanted with ^{84}Kr, and another with ^{129}Xe; in both cases, the energy of the implanted ions was 300 keV, the incident angle of the ions 0° and the total fluence 10^{17} at./cm^2. During implantation, the maximum sample temperatures of Kr and Xe were 103 °C and 142 °C, respectively, with an average current of 1.5 μA cm^{-2} and 1.75 μA cm^{-2}, respectively. The high implantation fluence was chosen for two reasons: firstly, to ensure that a sufficient quantity of Xe and Kr would be retained in the respective samples post-annealing, to be easily measured by ToF-ERDA; secondly, to replicate the high radiation damage present under high burnup conditions. It is important to note that the peak concentrations of Xe and Kr that resulted from using such high implantation fluence, were not themself representative of typical fission gas concentrations; nor was this the intention in this study. During both implantations, one half of each sample was masked using 50 μm Al foil, to preserve an unimplemented surface area on which reference measurements could later be performed. The implantations were simulated using 1D SDTrimSP version 6.09 [31,32], in dynamic mode, to obtain implanted-element profiles, sample-matrix damage profiles and sample-surface removal.

2.4. Elemental depth-profiling

ToF-ERDA measurements were conducted using the 5 MV NEC-5SDH-2 tandem accelerator at Uppsala University. The ToF-ERDA measurement system consists of a time-of-flight telescope, followed by a gas-ionisation chamber, so that both the energy and time-of-flight of recoiled particles are recorded in coincidence. For all measurements, a primary-ion beam of $^{197}Au^{+8}$ was used, with an energy of 40 MeV, incident at an angle of 67.5°to the sample surface-normal. The recoil-detection angle was set at 45° relative to the path of the primary-ion beam.

2.5. Thermal annealing

Samples were annealed at 1200 °C, for 9 h, in Ar atmosphere, using a Micro TF-6 high-temperature vertical furnace. The temperature was chosen as the highest that the furnace could stably maintain. The annealing time was chosen by applying literature values [33] for the diffusion pre-factor and activation energy for Xe and Kr in UO_2, at the chosen temperature, to the diffusion model presented in Section 2.6, and targeting a reduction of the peak concentrations of Xe and Kr by approximately 50%.

2.6. Diffusion model

The model used in the present work was based on Fick's second law [34], modified with a sink term, and the diffusion coefficient defined according to the well-known Arrhenius equation [35]. This model can be expressed in partial differential form as:

$$\frac{\partial C(x,t)}{\partial t} = D(T)\frac{\partial^2 C(x,t)}{\partial x^2} - \lambda C(x,t), \tag{1}$$

where $C(x,t)$ is the concentration of the diffusant in at.%, λ is the sink strength in units of s^{-1} and the diffusion coefficient

$$D(T) = D_0 \exp\left(-\frac{E_a}{kT}\right), \tag{2}$$

is in units of m^2/s, with D_0 being the pre-factor in m^2/s, E_a the activation energy of diffusion in eV, k the Boltzmann constant in eV/K and T the temperature in K. The model was solved numerically with Euler forward in the time domain and central difference in the space domain, with boundary conditions chosen to be:

$$\frac{\partial C(x,t)}{\partial x} = 0, \text{ at } x = 0, \tag{3}$$

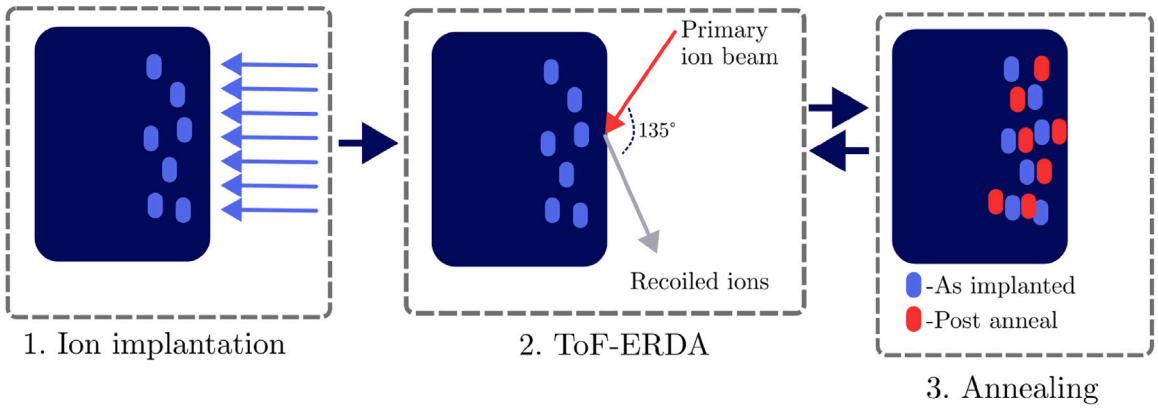

Fig. 1. A schematic depiction of the key steps employed in the present study: (1) The sample is subject to ion implantation, (2) the sample is analysed with ToF-ERDA to obtain depth-dependent concentration profile of the implanted elements, and (3) thermal annealing of the sample performed to induce migration of the implanted elements. Subsequently, analysis with ToF-ERDA is repeated to assess the effects of the annealing.

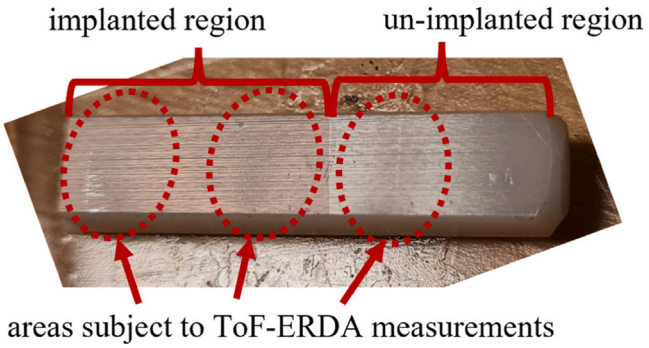

Fig. 2. ZrO_2 sample, following the implantation of Kr, annealing and ToF-ERDA measurements. Discolouration of the region subject to ion implantation can be seen, as can darkening of the areas on which Tof-ERDA was performed.

and

$$C(x,t) = 0, \text{ at } x = L, \tag{4}$$

where L is the length of the domain in nm. These boundary conditions dictate that the diffusant: can freely leave the surface of the sample; and will reach a concentration of zero at the end of the domain.

2.7. Determination of λ, D_0 and E_a

First-order estimates of λ, D_0 and E_a were obtained for the measured depth-dependent concentrations of Xe and Kr. This was performed by minimising the sum of the squared residuals (SSR) between the measured post-anneal concentration profiles for each element, and the predicted concentration profiles given by the model described in Section 2.6. The initial condition for the minimisation was set to be the respective depth-dependent elemental distribution of Xe or Kr, obtained from ToF-ERDA measurements pre-annealing. L was set to 600 nm in both cases, exceeding the greatest measurable extent of the implantation profiles by a factor of two. The initial values of E_a and D_0 were chosen to be to those found in [33]. The initial value of λ was set to 2.5×10^{-5} s^{-1}, this corresponding to the ~85% outgassing of the diffusant observed via measurement (see Section 3). The minimisation algorithm used was the Nelder–Mead [36,37] method, of the python *Scipy* library.

Since minimisation algorithms such as the Nelder–Mead method are prone to converge on local minima of the object function, and can be sensitive to the choice of starting parameters, an adaption of the bootstrapping method [38] was implemented to further optimise the values of D_0, E_a and λ obtained. The process scheme for this approach, which also provides uncertainty estimates on the derived coefficient values, is presented in Fig. 3. Following an initial minimisation using the starting values of D_0, E_a and λ previously stated, the minimisation was rerun 1000 times, but with starting values set to those obtained from the initial minimisation. For each run of the minimisation routine, normally distributed random-noise was added to each bin in the depth-dependent concentrations of Xe and Kr, post-anneal. The width of the sampled noise distribution was set independently for each bin, corresponding to the 1σ uncertainty. Subsequently, E_a and λ were re-fitted while keeping D_0 fixed. D_0 was kept fixed as only one data point, (D,T), is known, and Eq. (2) has two variables causing the system to be underdetermined. Fixing D_0 reduces the infinite solution space to one solution, which will be further evaluated in Section 4. The process of adding normally distributed noise to the concentrations of Xe and Kr, and re-fitting E_a and λ was repeated 1000 times while recording the values of E_a and λ each iteration; from which the mean and standard deviation were calculated. The mean of each parameter was taken as the fitted value with uncertainties equal to the standard deviation.

In Section 3, two predictions of the depth-dependent concentrations of Xe and Kr are presented: the first uses values of D_0 and E_0 obtained from the literature [33] along with λ set to 2.5×10^{-5} s^{-1}; the second employs the optimised parameters derived as described in this section. The first prediction of depth-dependant concentrations will be referred to as "Model:Initial", while the prediction employing the optimised parameters will be referred to as "Model:Optimised". The two predictions of the depth-dependent concentrations of Xe and Kr are shown to highlight the effectiveness of the optimisation.

3. Results

3.1. Elemental depth profiling measurements

Evaluation of the ToF-ERDA data was performed using the Potku software package [39]. A representative time-of-flight–energy coincidence plot obtained from the Kr implanted ZrO_2 sample is shown in Fig. 4(a), in which the high-energy, and short time-of-flight end of each track, represents recoil atoms originating from near the sample surface. Lower energies and longer flight times correspond to recoiled atoms originating from deeper within the sample. Evaluated elemental depth-profiles for the Kr and Xe implanted samples are shown in Fig. 4(b) and (c), respectively.

The expected signal tracks of O, Kr, Zr, Xe and Hf are observed in Fig. 4, in addition to scattered Au atoms from the primary-ion beam. Weak signals from Al can also be observed in Fig. 4, and although not shown in the figure, Cr signals were also in the measurement data. These signals were attributed to the halo of the primary-ion

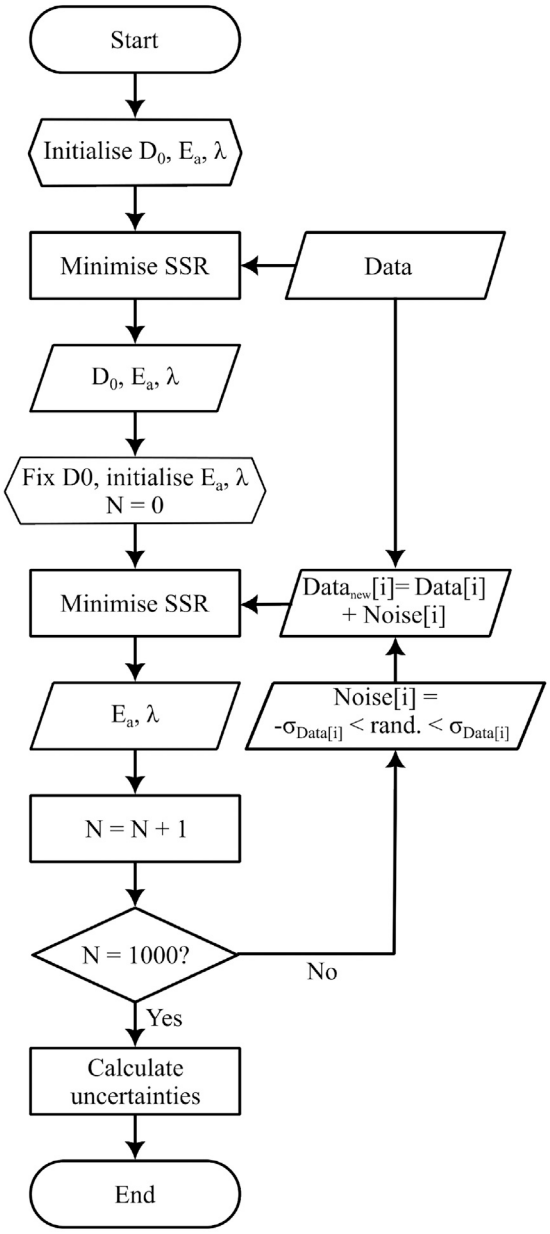

Fig. 3. The process scheme used to optimise and estimate uncertainties in D_0, E_a and λ. The parameters are initialised to a starting guess, and the SSR is minimised between the depth-dependant concentrations post anneal, and the model prediction. D_0, E_0 and λ is then re-initialised to the optimised values and a normally distributed noise is added to the depth-dependant concentrations. Subsequently, E_0 and λ is re-fitted, while keeping D_0 fixed, iterating 1000 times. From each iteration, E_0 and λ is recorded from which the mean and standard deviations are calculated. The mean and standard deviations of the parameters are utilised as the fitted values.

beam recoiling these elements from the sample holder. Al, Cr and Au are thus not regarded as present in the samples, and are therefore not included in the data evaluation procedure. Measured C, seen in Fig. 4, and not so readily observed N, appear in concentrations on the order of 0.5 at.%, these originating from the sample fabrication process. Hf is naturally co-occurring with Zr. The measured Hf:Zr ratios of (1.4 ± 0.7)% and (1.2 ± 0.7)% obtained from the evaluated data presented in Fig. 4(f) & (g), respectively, are consistent with expected values. Y, present as a stabilising dopant, could not be distinguished from Zr due to the similarity of these elements in atomic mass. The concentration of Y is therefore added to the Zr concentration in the evaluation procedure but, since this addition is consistent across all measurements, it does not influence the relative quantification of other elements.

As illustrated in Fig. 4, it was necessary to remove contributions to Kr-concentration depth-profiles that originated from Zr. This background subtraction was performed by evaluating the cut region for Kr in measurement data from the unimplanted side of the sample. This background profile was then normalised, depth-bin by depth-bin, to the ratio of the true Zr singles recorded from the implanted and unimplanted side of the sample. To avoid introducing statistical fluctuations, from the spares counts contributing to the background profile, a centred moving-average filter was applied to both the profile itself, and the profile of ratios used to normalise it. To be effective, this filter was designed with two key features: firstly, that it preserved the area of the profiles it was applied to; and secondly, that its application was modulated according to an error function about zero-depth, so as not to distort the surface edge of the distributions. The impact of this background correction was significant, shifting the mean depth of the evaluated Kr-concentration profiles from (1092 ± 29) to (869 ± 45) $\times 10^{15}$ at./cm^2 for the pre-anneal measurement, and from (1463 ± 9) to (1133 ± 150) $\times 10^{15}$ at./cm^2 for the post-anneal measurement. In terms of the evaluated areal densities for implanted Kr, background subtraction reduced values from (9.9 ± 0.4) to (5.7 ± 0.4) $\times 10^{16}$ at./cm^2 pre-annealing, and (3.8 ± 0.2) to (1.2 ± 0.2) $\times 10^{16}$ at./cm^2 post-annealing.

As the primary-ion beam used for ToF-ERDA can cause local heating of the surface area of the sample measured, outgassing of volatile species is possible. To evaluate the possibility of outgassing caused by such local heating, time stamps of the measurement data were used to compare the rates at which Xe and Kr signals were registered, relative to the rate of registered Zr signals, over the course of each measurement. No statistically significant shift in the relative signal rates could be observed in these evaluations and, as such, outgassing induced during measurements is considered negligible.

Uncertainties presented, on all measured concentrations, were derived from the counting statistics which contribute to the unnormalised result in each depth bin. These raw-result uncertainties were then propagated through the normalisation required to convert result values to at.%. In the case of concentration profiles which were background subtracted, uncertainties were additionally propagated through from the reference sample concentration profiles.

3.2. SDTrimSP simulations

Simulations employing SDTrimSP were performed with Xe and Kr in ZrO_2, to estimate the range distribution, damage distribution, sputtered ions and areal density. Coefficients for diffusion and outgassing were adjusted to match the simulated Kr- and Xe-concentration depth-profiles to those obtained from the pre-anneal ToF-ERDA measurements, as presented in Fig. 5, with simulated damage profiles overlid. Simulation results showed that ~20 nm of the sample surface was removed in the case of Kr implantation, and ~60 nm in the case of Xe implantation. Table 1 presents key values extracted from the SDTrimSP simulations, alongside the mean range and areal density obtained from the ToF-ERDA measurements. The mean range and areal density obtained from Model:Initial and Model:Optimised are also shown to allow for comparison.

A comparison between the SDTrimSP simulation results and the experimental ToF-ERDA measurements shows good agreement. The predicted mean implantation ranges are within 200 $\times 10^{15}$ at./cm^2 of the measured value, and the calculated areal density for Kr is within the uncertainty of the measurement while Xe is 0.5 $\times 10^{16}$ at./cm^2 smaller. It was also found that the peak damage implanted for Xe is about 1800, and the peak damage for Kr is about 1400. The mean damage was for Xe was found to be greater than Kr by a factor of 2. The measured implanted areal density was calculated by bin-wise integration of the measured elemental depth profile. In Fig. 5, the background-subtracted profile for Kr is shown.

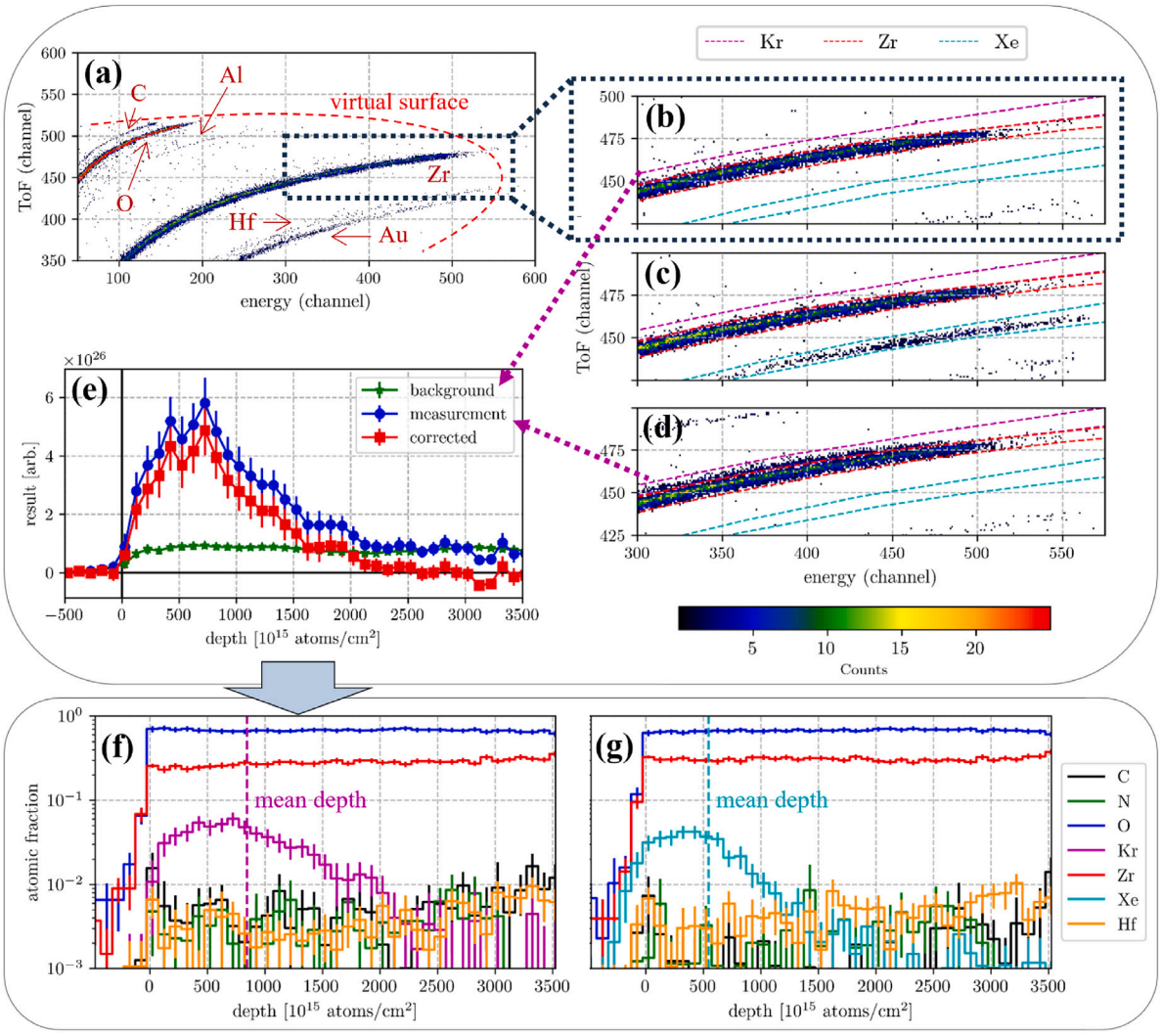

Fig. 4. ToF-ERDA results for the pre-annealed samples, illustrating the analysis methodology applied. (a) Time-of-flight–energy coincidence plot obtained from the analysis of unimplanted ZrO_2, with the virtual sample-surface indicated by the dashed line; one track can be seen for each element in the sample, as well as one track for Au, which results from scattering of the primary-ion beam. (b) Expansion of the area marked by the dotted squares in (a), with data cuts used for the evaluation of Kr-, Zr- and Xe-concentrations overlaid; it can be seen that signals from Zr fall within the cut region for Kr, but that the cut region for Xe is free from any such background. (c) and (d) The same region of the histogram shown (b), but for data collected from Kr- and Xe-implanted samples respectively. (e) Background subtraction performed on raw evaluation results for Kr, in which the background profile is generated from Zr signals which fall within the cut region for Kr in the unimplanted sample. (f) and (g) Evaluated elemental depth-profiles for Kr- and Xe-implanted ZrO_2 respectively, with the mean of each implanted depth-distribution indicated by the dashed lines; the depth profile for Kr is the background subtracted distribution shown in (e), following normalisation; no background subtraction was necessary to correct the measured Xe depth distribution, and as such the elemental depth profiles shown in (g) result from a direct evaluation of the data presented in (c).

Table 1
The key elements extracted from the SDTrimSP simulations showing the sputtered depth, mean damage in displacements per atom (dpa) as predicted by SDTrimSP, mean range as predicted by SDTrimSP and as measured by ToF-ERDA, and the areal densities calculated with SDTrimSP and measured by ToF-ERDA. Background was removed from the measurement before the calculation of areal density.

Quantity	Unit	Source	ZrO_2 + Xe	ZrO_2 + Kr
Sputtered depth	nm	SDTrimSP	56.9	18.5
Mean damage	dpa	SDTrimSP	403	196
Mean range	10^{15} at./cm^2	SDTrimSP	702	920
		ToF-ERDA pre-anneal	537 ± 30	869 ± 46
		ToF-ERDA post-anneal	740 ± 71	1133 ± 150
		Model:Initial	928	1214
		Model:Optimised	922	1217
Areal density	10^{16} at./cm^2	SDTrimSP	3.1	5.6
		ToF-ERDA pre-anneal	3.8 ± 0.2	5.7 ± 0.4
		ToF-ERDA post-anneal	0.7 ± 0.1	1.2 ± 0.2
		Model:Initial	1.56	2.34
		Model:Optimised	0.68	0.97

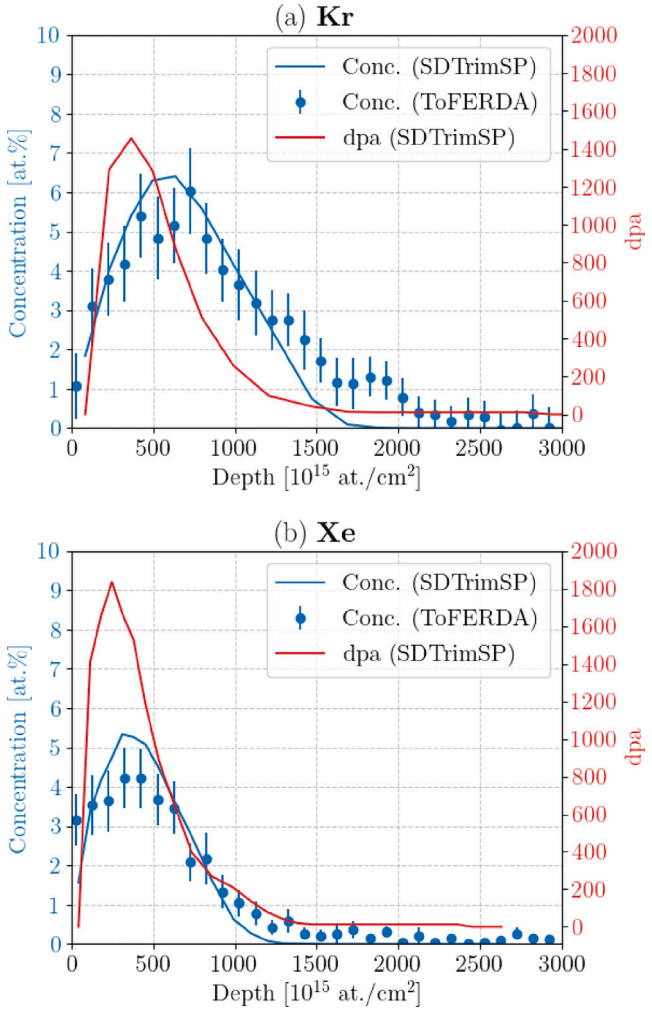

Fig. 5. The depth depended concentration- and damage-profiles, as produced from SDTrimSP simulations, of the implantation of (a) Kr and (b) Xe in ZrO_2. The respective depth- dependent concentration-profiles obtained by ToF-ERDA are also shown for comparison. In the case of the Kr simulation, values used for diffusion coefficients 1 and 2 were 8×10^{16} and 50, respectively; where as in the case of the Xe simulation values used were 1×10^{16} and 200.

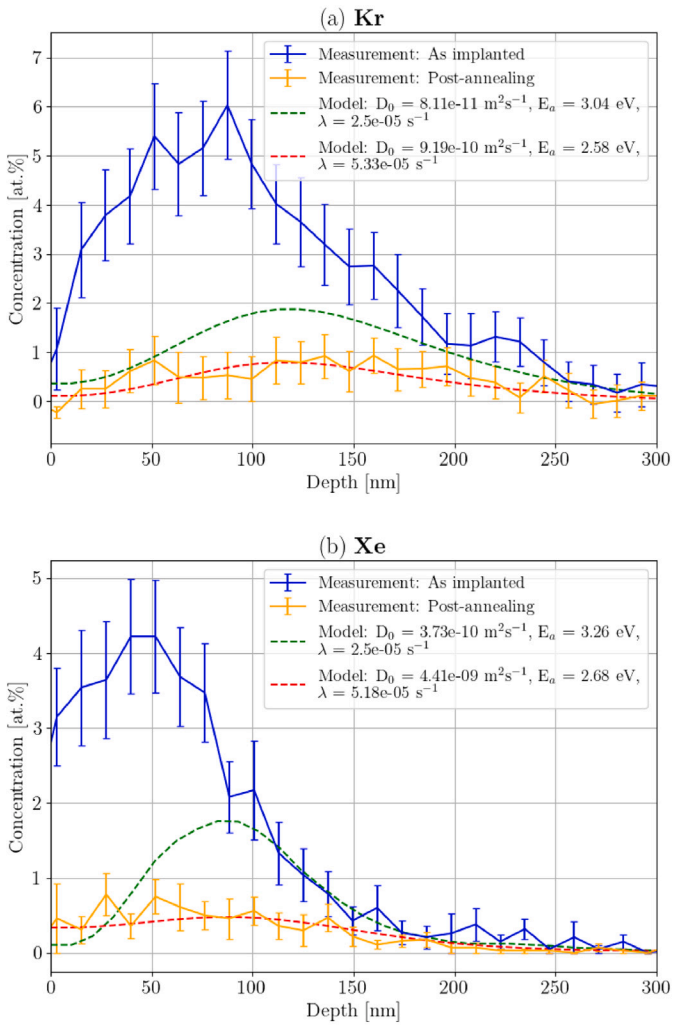

Fig. 6. Calculations of the thermal diffusion of (a) Kr and (b) Xe as a first estimate with diffusion-coefficient parameters from a study made in UO_2 [33], referred to as Model:Initial, and with optimised parameters as described in Section 2.6, referred to as Model:Optimised. Depth-dependent concentration profiles, as measured by ToF-ERDA, for both pre- and post-annealed samples are also shown, with background subtraction performed for the Kr implanted sample. The depth scale was re-scaled from at/cm^2 to nm utilising the number density at the given depth as simulated by SDTrimSP.

3.3. Extracting diffusion coefficients

Fig. 6 presents the measured depth-dependent concentrations of the diffusants, pre- and post-annealing, alongside the corresponding predictions derived from the model described in Section 2.6. The depth scale was converted from at./cm^2 to nm re-scaling each bin by the number density at the given depth. The number density as a function of depth was interpolated from SDTrimSP simulations. Two sets of predictions are shown in Fig. 6: one using values of D_0 and E_a, obtained from the literature [33] and λ equal to 2.5×10^{-5} s^{-1}, referred to as Model:Initial; the other using optimised parameters of E_a, D_0 and λ, referred to as Model:Optimised. The parameters employed in Model:Initial and Model:Optimised is shown in Table 2. The outgassing of implanted ions during annealing was calculated from the areal densities of the ToF-ERDA measurement, pre- and post-annealing, and was found to be (85 ± 7)% of the Kr and (83 ± 7)% of the Xe. The outgassing during annealing, within the uncertainty of the measurement, is therefore equal and suggests that the loss of species during annealing is governed by the same mechanism. From the measured outgassing, an estimation of λ was made by calculating the sink strength required to remove 85% of the diffusant during annealing, yielding a value of λ=2.5×10^{-5} s^{-1}. As shown in Table 1, Model:Initial predicts areal densities of 2.34×10^{16} at./cm^2 and 1.56×10^{16} at./cm^2 for Kr and Xe, respectively, whereas Model:Optimised yielded predictions of 0.97×10^{16} at./cm^2 and 0.68×10^{16} at./cm^2 for Kr and Xe, respectively. The areal densities calculated by the model and the areal densities obtained using ToF-ERDA, agree within the measurement uncertainty for the calculation using the optimised parameters. In contrast, the calculation employing parameters from [33] overestimates the areal density due to the lower sink strength.

Fig. 7 shows the distribution of E_a and λ, keeping D_0 fixed, while varying the data, from which the uncertainties in E_a and λ were found. The distributions of E_0 and λ show Gaussian behaviour, with some bins that are more preferred than others. The convergence rate for both cases was ~80%.

4. Discussion

Previous studies [25] demonstrated that annealing at 800 °C for 1 h produces changes smaller than the experimental uncertainty. In contrast, the current study shows changes that significantly exceed

Table 2
The parameters used in the model from a previous study [33], referred to as Model:Initial, and optimised parameters derived by minimising the SSR of the model prediction, referred to as Model:Optimised. Uncertainties quoted for the optimised parameters are derived from bootstrap resampling. The outgassing of diffusants during annealing is also shown, with uncertainties calculated from counting statistics.

Ion	Outgassing	Source	E_a [eV]	D_0 [10^{-11} m^2/s]	λ [10^{-5}/s]
Kr	85 ± 7%	Model:Initial	3.04 ± 0.51	8.11	2.5
		Model:Optimised	2.58 ± 0.08	91.9	5.33 ± 0.18
Xe	83 ± 7%	Model:Initial	3.26 ± 0.35	37.3	2.5
		Model:Optimised	2.68 ± 0.08	441	5.20 ± 0.19

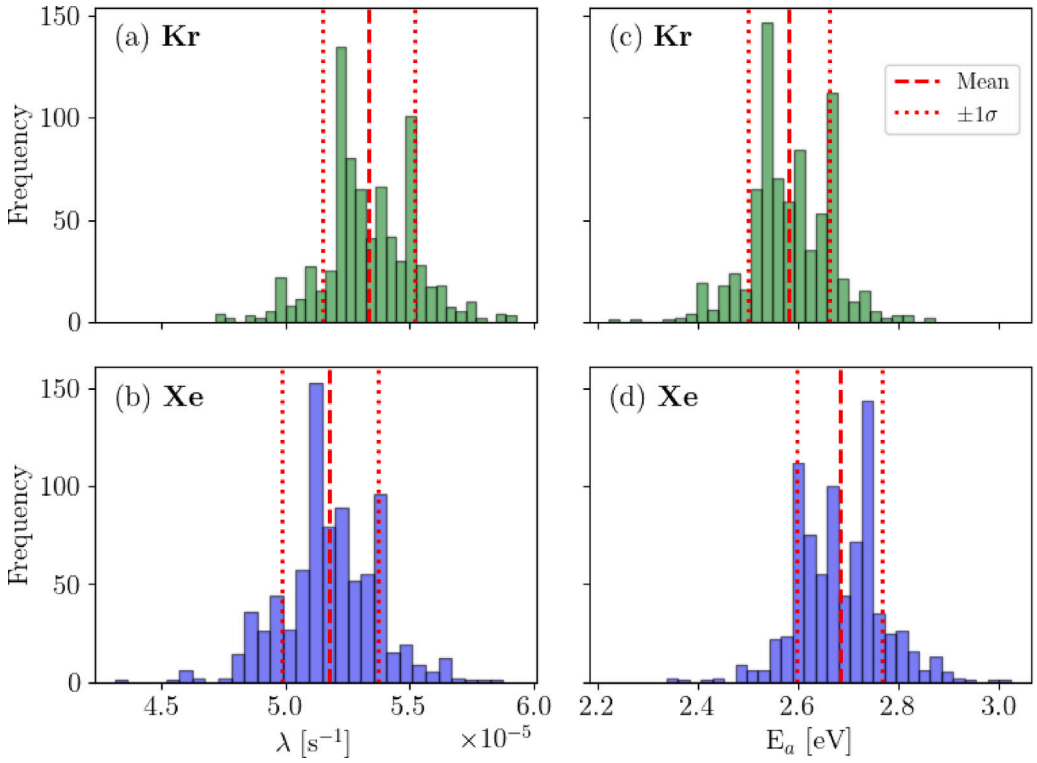

Fig. 7. The distribution of fitted parameters when employing bootstraping for (a) Kr and (b) Xe, varying the data by the uncertainty within each bin. From these distributions, the values of λ and E_a were taken to be the respective means, and the uncertainties on these values to be the respective standard deviations.

statistical uncertainties, enabling a more detailed analysis of the diffusion mechanisms. As shown in Table 2, approximately 85% of the implanted atoms were outgassed during annealing, and the similarity in concentration outgassed between Kr and Xe suggests a common diffusion and release mechanism in ZrO_2. This mechanism is independent of atomic mass and size, aligning with previous studies obtained for low-concentration Xe and Kr in UO_2 [33]. Applying the optimised values presented in Table 2 to Eq. (2) yields first-order approximations of thermal-diffusion coefficients of Kr and Xe in ZrO_2 at 1200 °C as $(1.36 \pm 0.87) \times 10^{-19}$ m^2/s and $(2.94 \pm 1.96) \times 10^{-19}$ m^2/s. These thermal-diffusion coefficients are two orders of magnitude larger than those previously found for Kr and Xe in UO_2 [33,40]. Previous work [41] suggests that implantation fluences above 3×10^{16} at./cm^2 cause solid and fluid noble gas inclusions. The fluence employed in this study was 10^{17} at./cm^2, resulting in the high-damage to the sample matrix seen in Fig. 5. Although it is difficult to identify the dominant mechanism from a single experimental set, this high damage, combined with the considerably higher diffusion coefficients compared to [33,40], suggest that the diffusion process observed in the present work is irradiation-enhanced, rather than purely thermal [42]. As shown in Fig. 5, the mean damage caused by Xe is approximately twice that of Kr, which contributes to the higher diffusion coefficient derived for Xe in this study. Table 1 also shows that the mean range following annealing was increased by ~ 200 × 10^{15} at./cm^2. The slight shift in mean range further supports that the diffusion is not only thermal, as the mean range would be closer to the centre of the domain if thermal-diffusion dominates. Atomic diffusion through the vacancy mechanism is governed by both the concentration of vacancies and the vacancy migration energy, meaning that if the concentration of vacancies is larger, the diffusion coefficient of atoms in the matrix will be larger. Thus, the mechanism of diffusion of Kr and Xe in this work is mostly irradiation-enhanced. Using a fluence on the order of 10^{17} at./cm^2 of Kr or Xe creates damage on the order of 1000 dpa which is realistic for fuel in reactor environments [43]. Thus, the implantation conditions used here are representative of operational damage states.

The agreement between the modelled and the measured depth-dependent concentration profiles, presented in Fig. 6, is seen to be excellent for both the Xe and Kr implanted samples. Being critical of this agreement from the perspective of the empirical data sets, it could be supposed that the statistical uncertainties on the measured concentrations are slightly overestimated, as only ~10% of the values lie more than 1σ from the corresponding model prediction. It must also be considered that systematic uncertainties are not accounted for in the measured data; other than those relating to the background subtraction performed on the Kr concentration profile. ToF-ERDA is known to be influenced by multiple and plural scattering effects, particularly when analysing samples with heavy matrices [44–46], which limits the probing depth and degrades the depth resolution. However, as multiple and plural scattering effects exhibit similar magnitudes across samples of similar compositions, accurate comparative analysis can be performed

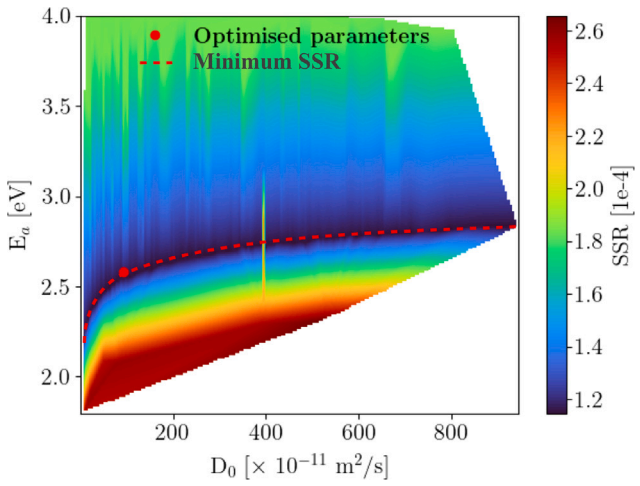

Fig. 8. The SSR surface created by varying the initial guess of D_0 and E_a, showing that there exists an infinite number of combinations which minimise the result. The optimised parameters for Kr, as derived in this work, are shown for reference.

despite potentially inaccurate absolute values. Therefore, ToF-ERDA remains a powerful tool for comparative studies, as demonstrated in this work. The main discrepancy with the model prediction is that the mean range after annealing is over-estimated by $\sim 100 \times 10^{15}$ at./cm^2 as seen in Table 1. This discrepancy can be attributed to the lack of an atom-drift term [47] in the diffusion model. Species deeper in the sample should diffuse towards the surface, altering the shape of the distribution in the surface area. A gas atom drift term could therefore be added to Fick's law to modify the diffusion equation to account for the drift mechanism. The physical explanation of the gas atom drift effect is that fission fragments cause lattice distortions, which cause swelling. The swelling, in turn, causes stress on each grain. As the grain boundaries interlink, a stress gradient forms which drifts dislocations in the direction of the gradient. As the dislocations move, gas atoms are dragged in the same direction [48]. The magnitude of the drift effect is proportional to the burn-up in the fuel and follows dislocations [11]. The drift effect of the gas atoms is dominant at temperatures below 1000 °C, though it continues to contribute to atomic transport at higher temperatures.

It is important to note that as one data point was utilised in this work, there exists an infinite number of combinations of D_0 and E_a that minimises the SSR, and yields the correct total diffusion coefficient, D. The infinite solution space stems from the fact that Eq. (2) has two variables, and with only one data point, the system is underdetermined. Hence, the value of D_0 and E_a will depend on the initial guess of D_0 and E_a. The infinite solution-space can be visualised by minimising the SSR while varying the initial guess, and is shown for Kr in Fig. 8, with the optimised parameters derived in this work marked. The minimum SSR line, marked in Fig. 8, represents the infinite number of solutions, all of which minimise the SSR. Therefore, the initial guess of D_0 and E_a was set to the values reported in [33], as a physically meaningful estimate was required to identify the most physically relevant minimum. D_0 was also held fixed during re-iteration to ensure that there only existed one unique solution to Eq. (2).

Fig. 8 also reveals that there exists many minima near, and around the optimised parameters. To ensure that the optimisation algorithm finds the correct minima, other optimisation algorithms could be tested to evaluate which method converges more rapidly. The current method is prone to find local minima, and could affect which parameters the model finds during optimisation. To uniquely determine D_0 and E_a, an additional measurement at a different temperature would be required. More measurements, applying a range of different implantation fluences, annealing temperatures and annealing times should be performed to yield more data points such that interpolation according to the Arrhenious law can be performed. By having more data points on the Arrhenious curve, the exact values of D_0 and E_a can be found.

5. Conclusions

This work aimed to evaluate the effectiveness of the analysis of diffusion of gaseous fission products with medium-energy ion implantation combined with ToF-ERDA, and the effectiveness of modelling the diffusion of gaseous fission products using a model based on Fick's law. First-order approximations of the diffusion coefficients were derived and were found to be greater than those previously found, due to the atomic diffusion through the vacancy mechanism. It was found that Xe and Kr diffuse in highly irradiated samples using the same mechanism. The model, based on Fick's law, can successfully predict the diffusion of the implanted species but will need further tests to conclude the accuracy of the predictions. Good agreement with pervious studies were found with regards to the activation energy and the thermal pre-factor, though no direct comparison was possible.

It was shown that medium-energy ion implantation in combination with ToF-ERDA is a powerful technique to study the diffusion of volatile fission products. The method has now been tested in two cases, namely this work and previously by Frost et al. [25]. In both cases ToF-ERDA produces reliable data to analyse the diffusion of volatile fission products without the need to apply destructive measurement techniques or use irradiated samples. The combination of medium-energy ion implantation and ToF-ERDA thus offers quantitative analysis of the diffusion of implanted species as it is not destructive since it utilises high energy ion beams tens of MeV, making sputter yields negligible. The data from ToF-ERDA can be directly translated from non-relativistic scattering and therefore provide quantitative depth-profiling.

Declaration of competing interest

The authors declare that they have no known competing financial interests or personal relationships that could have appeared to influence the work reported in this manuscript.

Acknowledgements

The authors gratefully acknowledge the financial support of the Swedish Centre for Nuclear Technology (SKC, Svenskt Kärntekniskt Centrum), Sweden under grant number SKC-2024-B, the Swedish Research Council (VR, Vetenskapsrådet), Sweden under contract number VR-RFI-2019-00191 supporting accelerator operation at the Tandem Laboratory, the Swedish Energy Agency (Energimyndigheten), Sweden under grant number P2023-01348 in the Nuclear Materials Platform (NuMaP) and The Swedish Foundation for Strategic Research (SSF, Stiftelsen för Strategisk Forskning), Sweden within the SUNRISE Centre under grant number ARC19-0043. The authors acknowledge the use of the MyFab cleanroom facility at Uppsala University for access to the furnace equipment. The authors would also like to thank Kyle Johnson for his time in discussing this work, and Dzemil Adrovic for his assistance in the laboratory.

References

[1] T.W. Kerlin, B.R. Upadhyaya, Chapter 6 - Fission product poisoning, in: T.W. Kerlin, B.R. Upadhyaya (Eds.), Dynamics and Control of Nuclear Reactors, Academic Press, 2019, pp. 57–71.
[2] H. Bailly, D. Menessier, C. Prunier, The Nuclear Fuel of Pressurized Water Reactors and Fast Reactors Design and Behaviour, Commissariat a l'Energie Atomique, 1999.
[3] B.G. Childs, Fission product effects in uranium dioxide, J. Nucl. Mater. 9 (3) (1963) 217–244, http://dx.doi.org/10.1016/0022-3115(63)90141-7.
[4] J. Turnbull, C.A. Friskney, J. Findlay, F. Johnson, A.J. Walter, The diffusion coefficients of gaseous and volatile species during the irradiation of uranium dioxide, J. Nucl. Mater. 107 (1982) 168–184, http://dx.doi.org/10.1016/0022-3115(82)90419-6.

[5] T. Allen, J. Busby, M. Meyer, D. Petti, Materials challenges for nuclear systems, Mater. Today 13 (12) (2010) 14–23, http://dx.doi.org/10.1016/S1369-7021(10)70220-0.

[6] G.T. Lawrence, A review of the diffusion coefficient of fission-product rare gases in uranium dioxide, J. Nucl. Mater. 71 (2) (1978) 195–218, http://dx.doi.org/10.1016/0022-3115(78)90418-X.

[7] M. Gerardin, E. Gilabert, D. Horlait, M.-F. Barthe, G. Carlot, Experimental study of the diffusion of Xe and Kr implanted at low concentrations in UO2 and determination of their trapping mechanisms, J. Nucl. Mater. 556 (2021) 153174, http://dx.doi.org/10.1016/j.jnucmat.2021.153174.

[8] P. Peres, S.-Y. Choi, F. Desse, P. Bienvenu, I. Roure, Y. Pipon, C. Gaillard, N. Moncoffre, L. Sarrasin, D. Mangin, Dynamic SIMS for materials analysis in nuclear science, J. Vac. Sci. Technol. B 36 (3) (2018) 03F117, http://dx.doi.org/10.1116/1.5017027.

[9] J. Rest, M.W.D. Cooper, J. Spino, J.A. Turnbull, P. Van Uffelen, C.T. Walker, Fission gas release from UO2 nuclear fuel: A review, J. Nucl. Mater. 513 (2019) 310–345, http://dx.doi.org/10.1016/j.jnucmat.2018.08.019.

[10] M. Tonks, D. Andersson, R. Devanathan, R. Dubourg, A. El-Azab, M. Freyss, F. Iglesias, K. Kulacsy, G. Pastore, S.R. Phillpot, M. Welland, Unit mechanisms of fission gas release: Current understanding and future needs, J. Nucl. Mater. 504 (2018) 300–317, http://dx.doi.org/10.1016/j.jnucmat.2018.03.016.

[11] J.H. Shea, An improved model of fission gas atom transport in irradiated uranium dioxide, J. Nucl. Mater. 501 (2018) 302–311, http://dx.doi.org/10.1016/j.jnucmat.2018.01.009.

[12] K. Taketani, K. Ikawa, Release of xenon from sintered UO2 at low temperatures, J. Nucl. Sci. Technol. 4 (12) (1967) 589–594, http://dx.doi.org/10.1080/18811248.1967.9732814.

[13] R.J. White, M.O. Tucker, A new fission-gas release model, J. Nucl. Mater. 118 (1) (1983) 1–38, http://dx.doi.org/10.1016/0022-3115(83)90176-9.

[14] H. György, S. Czifrus, The utilization of thorium in Generation IV reactors, Prog. Nucl. Energy 93 (2016) 306–317, http://dx.doi.org/10.1016/j.pnucene.2016.09.007.

[15] W.J. Carmack, D.L. Porter, Y.I. Chang, S.L. Hayes, M.K. Meyer, D.E. Burkes, C.B. Lee, T. Mizuno, F. Delage, J. Somers, Metallic fuels for advanced reactors, J. Nucl. Mater. 392 (2) (2009) 139–150, http://dx.doi.org/10.1016/j.jnucmat.2009.03.007, Nuclear Fuels and Structural Materials 2.

[16] Y. Guo, C. Yu, J. Lin, C. Wang, C. Ren, B. Sun, P. Huai, R. Xie, X. Ke, Z. Zhu, H. Xu, Pressure-induced structural transformations and polymerization in ThC2, Sci. Rep. 7 (2017) http://dx.doi.org/10.1038/srep45872.

[17] I.R. Shein, A.L. Ivanovskii, First-principles study of structural, elastic and electronic properties of thorium dicarbide (ThC2) polymorphs, J. Nucl. Mater. 393 (1) (2009) 192–196, http://dx.doi.org/10.1016/j.jnucmat.2009.06.004.

[18] A.L. Bowman, N.H. Krikorian, G.P. Arnold, T.C. Wallace, N.G. Nereson, The crystal structures of ThC2, Acta Crystallogr. Sect. B Struct. Crystallogr. Cryst. Chem. 24 (1968) 1121–1123, http://dx.doi.org/10.1107/S056774086800378X.

[19] M. Ahmed Mohammed, S. Razaq, W. Abdulridha, Structural, optical, electrical and gas sensor properties of ZrO 2 thin films prepared by Sol-Gel technique, NeuroQuantology 18 (3) (2020) 22–27, http://dx.doi.org/10.14704/nq.2020.18.3.NQ20146.

[20] C.P. Kempter, N.H. Krikorian, Some properties of thorium monocarbide and dicarbide, J. the Less Common Met. 4 (3) (1962) 244–251, http://dx.doi.org/10.1016/0022-5088(62)90071-1.

[21] M. Yoshiya, M. Matsumoto, A. Harada, M. Takeuchi, H. Matsubara, Thermal conductivity of zirconia for thermal barrier coatings: A perturbed molecular dynamics study, in: The Science of Engineering Ceramics III, in: Key Engineering Materials, vol. 317, Trans Tech Publications Ltd, 2006, pp. 521–524, http://dx.doi.org/10.4028/www.scientific.net/KEM.317-318.521.

[22] Z. Liao, P. Huai, W. Qiu, X. Ke, W. Zhang, Z. Zhu, Lattice dynamics and lattice thermal conductivity of thorium dicarbide, J. Nucl. Mater. 454 (1) (2014) 142–148, http://dx.doi.org/10.1016/j.jnucmat.2014.07.060.

[23] D. Pérez Daroca, A.M. Llois, H.O. Mosca, Diffusion in thorium carbide: A first-principles study, J. Nucl. Mater. 467 (2015) 572–575, http://dx.doi.org/10.1016/j.jnucmat.2015.10.011.

[24] I. Cohen, B.E. Schaner, A metallographic and X-ray study of the UO2-ZrO2 system, J. Nucl. Mater. 9 (1) (1963) 18–52, http://dx.doi.org/10.1016/0022-3115(63)90166-1.

[25] R.J.W. Frost, D.A. Lopes, K.D. Johnson, S. Patnaikb, J. Oscarsson, M. Sortica, P. Peterssona, D. Primetzhofer, Evaluating the diffusion of kr in uo2 and adopttm using time-of-flight elastic recoil detection analysis (tof-erda), Journal of Nuclear Science and Technology 62 (3) (2025) 243–249, http://dx.doi.org/10.1080/00223131.2024.2423639.

[26] C. Jiang, X.-Y. Liu, K.E. Sickafus, First-principles prediction of the thermodynamic stability of xenon in monoclinic, tetragonal, and yttrium-stabilized cubic ZrO_2, Phys. Rev. B 83 (2011) 052103, http://dx.doi.org/10.1103/PhysRevB.83.052103.

[27] H.Y. Xiao, W.J. Weber, Y. Zhang, First-principles study of the stability and migration of Kr, I and Xe in ZrO2, J. Nucl. Mater. 446 (1) (2014) 172–177, http://dx.doi.org/10.1016/j.jnucmat.2013.11.044.

[28] K.A. Terrani, N.A. Capps, M.J. Kerr, C.A. Back, A.T. Nelson, B.D. Wirth, S.L. Hayes, C.R. Stanek, Accelerating nuclear fuel development and qualification: Modeling and simulation integrated with separate-effects testing, J. Nucl. Mater. 539 (2020) 152267, http://dx.doi.org/10.1016/j.jnucmat.2020.152267.

[29] D.L. Bourell, Parimal, W. Kaysser, Sol–Gel synthesis of nanophase yttria-stabilized tetragonal zirconia and densification behavior below 1600 K, J. Am. Ceram. Soc. 76 (3) (1993) 705–711, http://dx.doi.org/10.1111/j.1151-2916.1993.tb03663.x.

[30] P. Ström, D. Primetzhofer, Ion beam tools for nondestructive in-situ and in-operando composition analysis and modification of materials at the Tandem Laboratory in Uppsala, J. Instrum. 17 (04) (2022) P04011, http://dx.doi.org/10.1088/1748-0221/17/04/P04011.

[31] A. Mutzke, R. Schneider, W. Eckstein, R. Dohmen, K. Schmid, U. Toussaint, et al., SDTrimSP Version 6.00 (IPP 2019-02), Max-Planck-Institut für Plasmaphysik, Garching, 2019, http://dx.doi.org/10.17617/2.3026474.

[32] P.S. Szabo, D. Weichselbaum, H. Biber, C. Cupak, A. Mutzke, R.A. Wilhelm, F. Aumayr, Graphical user interface for SDTrimSP to simulate sputtering, ion implantation and the dynamic effects of ion irradiation, Nucl. Instrum. Methods Phys. Res. Sect. B: Beam Interact. Mater. At. 522 (2022) 47–53, http://dx.doi.org/10.1016/j.nimb.2022.04.008.

[33] M. Gérardin, E. Gilabert, D. Horlait, M.-F. Barthe, G. Carlot, Diffusion of Xe and Kr implanted at low concentrations in UO2 as a function of temperature – An experimental study, J. Nucl. Mater. 582 (2023) 154476, http://dx.doi.org/10.1016/j.jnucmat.2023.154476.

[34] A. Fick, Ueber diffusion, Ann. Phys., Lpz. 170 (1) (1855) 59–86.

[35] S. Arrhenius, Über die reaktionsgeschwindigkeit bei der inversion von rohrzucker durch säuren, Z. Phys. Chem. 4 (1) (1889) 226–248.

[36] P. Virtanen, R. Gommers, T.E. Oliphant, M. Haberland, T. Reddy, D. Cournapeau, E. Burovski, P. Peterson, W. Weckesser, J. Bright, S.J. van der Walt, M. Brett, J. Wilson, K.J. Millman, N. Mayorov, A.R.J. Nelson, E. Jones, R. Kern, E. Larson, C.J. Carey, I. Polat, Y. Feng, E.W. Moore, J. VanderPlas, D. Laxalde, J. Perktold, R. Cimrman, I. Henriksen, E.A. Quintero, C.R. Harris, A.M. Archibald, A.H. Ribeiro, F. Pedregosa, P. van Mulbregt, A. Vijaykumar, A.P. Bardelli, A. Rothberg, A. Hilboll, A. Kloeckner, A. Scopatz, A. Lee, A. Rokem, C.N. Woods, C. Fulton, C. Masson, C. Häggström, C. Fitzgerald, D.A. Nicholson, D.R. Hagen, D.V. Pasechnik, E. Olivetti, E. Martin, E. Wieser, F. Silva, F. Lenders, F. Wilhelm, G. Young, G.A. Price, G.-L. Ingold, G.E. Allen, G.R. Lee, H. Audren, I. Probst, J.P. Dietrich, J. Silterra, J.T. Webber, J. Slavič, J. Nothman, J. Buchner, J. Kulick, J.L. Schönberger, J.V. de Miranda Cardoso, J. Reimer, J. Harrington, J.L.C. Rodríguez, J. Nunez-Iglesias, J. Kuczynski, K. Tritz, M. Thoma, M. Newville, M. Kümmerer, M. Bolingbroke, M. Tartre, M. Pak, N.J. Smith, N. Nowaczyk, N. Shebanov, O. Pavlyk, P.A. Brodtkorb, P. Lee, R.T. McGibbon, R. Feldbauer, S. Lewis, S. Tygier, S. Sievert, S. Vigna, S. Peterson, S. More, T. Pudlik, T. Oshima, T.J. Pingel, T.P. Robitaille, T. Spura, T.R. Jones, T. Cera, T. Leslie, T. Zito, T. Krauss, U. Upadhyay, Y.O. Halchenko, Y. Vázquez-Baeza, SciPy 1.0: fundamental algorithms for scientific computing in Python, Nature Methods 17 (3) (2020) 261–272, http://dx.doi.org/10.1038/s41592-019-0686-2.

[37] J.A. Nelder, R. Mead, A simplex method for function minimization, Comput. J. 7 (4) (1965) 308–313, http://dx.doi.org/10.1093/comjnl/7.4.308.

[38] B. Efron, R. Tibshirani, The bootstrap method for assessing statistical accuracy, Behaviormetrika 12 (17) (1985) 1–35, http://dx.doi.org/10.2333/bhmk.12.17_1.

[39] K. Arstila, J. Julin, M.I. Laitinen, J. Aalto, T. Konu, S. Kärkkäinen, S. Rahkonen, M. Raunio, J. Itkonen, J.-P. Santanen, T. Tuovinen, T. Sajavaara, Potku – New analysis software for heavy ion elastic recoil detection analysis, Nucl. Instrum. Methods Phys. Res. B 331 (2014) 34–41, http://dx.doi.org/10.1016/j.nimb.2014.02.016, 11th European Conference on Accelerators in Applied Research and Technology.

[40] C. Matthews, R. Perriot, M.W.D. Cooper, C.R. Stanek, D.A. Andersson, Cluster dynamics simulation of xenon diffusion during irradiation in UO2, J. Nucl. Mater. 540 (2020) 152326, http://dx.doi.org/10.1016/j.jnucmat.2020.152326.

[41] C. Degueldre, M. Pouchon, M. Döbeli, K. Sickafus, K. Hojou, G. Ledergerber, S. Abolhassani-Dadras, Behaviour of implanted xenon in yttria-stabilised zirconia as inert matrix of a nuclear fuel, J. Nucl. Mater. 289 (1) (2001) 115–121, http://dx.doi.org/10.1016/S0022-3115(00)00690-5, Symp. on Fabrication and Properties of Ceramics for Fusion Energy.

[42] G.S. Was, Radiation-enhanced diffusion and defect reaction rate theory, Fundamentals of Radiation Materials Science: Metals and Alloys, Springer New York, New York, NY, 2017, pp. 207–252, http://dx.doi.org/10.1007/978-1-4939-3438-6_5.

[43] H. Matzke, Radiation damage in nuclear fuel materials, in: Solid State Phenomena, Vol. 30–31, Trans Tech Publications, Ltd., 1992, pp. 355–366, http://dx.doi.org/10.4028/www.scientific.net/ssp.30-31.355.

[44] D.A. Eastham, Plural and multiple scattering of heavy ions in solids by Monte Carlo methods, Nucl. Instrum. Methods 125 (2) (1975) 277–283, http://dx.doi.org/10.1016/0029-554X(75)90279-7.

[45] K. Arstila, T. Sajavaara, J. Keinonen, Monte Carlo simulation of multiple and plural scattering in elastic recoil detection, Nucl. Instrum. Methods Phys. Res. B 174 (1) (2001) 163–172, http://dx.doi.org/10.1016/S0168-583X(00)00435-3.

[46] E. Pitthan, M.V. Moro, S.A. Corrêa, D. Primetzhofer, Assessing boron quantification and depth profiling of different boride materials using ion beams, Surf. Coat. Technol. 417 (2021) 127188, http://dx.doi.org/10.1016/j.surfcoat.2021.127188.

[47] A.G. Kesarev, V.V. Kondratyev, I.L. Lomaev, On the theory of atomic diffusion after ion implantation, Phys. Met. Met. 119 (2018) 1101–1106, http://dx.doi.org/10.1134/S0031918X18110078.

[48] A.H. Cottrell, D.L. Dexter, Dislocations and plastic flow in crystals, Am. J. Phys. 22 (4) (1954) 242–243, http://dx.doi.org/10.1119/1.1933704.